We examined the cellular localization of TAT-1 by expressing a TAT-1 fusion protein tagged at its carboxyl terminus with a FLAG epitope under the control of the *tat-1* gene promoter ($P_{tat\text{-}1}$*tat-1::flag*). Several extrachromosomal transgene arrays and an integrated transgene (*smIs142*) carrying $P_{tat\text{-}1}$*tat-1::flag* were generated and all fully rescued the missing cell phenotype of the *tat-1(tm1034)* mutant (table S2). *smIs142* also partially rescued the germ cell PS exposure defect of the *tat-1(tm1034)* mutant (fig. S7). Immunostaining of gonads from the *smIs142* animals using a monoclonal antibody (M2) to the FLAG epitope revealed that TAT-1 localizes predominantly on the plasma membrane (Fig. 4).

Class IV P-type ATPases have been suggested to promote translocation of aminophospholipids [PS and phosphatidylethanolamine (PE)] from the outer leaflet to the inner leaflet of plasma membrane and thus may have a role in maintaining asymmetrical distribution of PS and PE on the lipid bilayer (*3*, *22*, *23*). However, in multicellular organisms, multiple members of this ATPase family exist (at least 14 were identified in mammals), which prevents genetic analysis of their in vivo functions (*3*, *22*, *24*). Our findings thus provide important in vivo evidence that a member of the aminophospholipid translocase family is involved in maintaining PS asymmetry on plasma membrane and that disruption of such PS asymmetry can result in indiscriminate removal of affected cells by neighboring phagocytes.

References and Notes

1. M. E. Auland, B. D. Roufogalis, P. F. Devaux, A. Zachowski, *Proc. Natl. Acad. Sci. U.S.A.* **91**, 10938 (1994).
2. J. K. Paterson *et al.*, *Biochemistry* **45**, 5367 (2006).
3. D. L. Daleke, *J. Lipid Res.* **44**, 233 (2003).
4. Materials and methods are available on *Science* Online.
5. X. Wang *et al.*, *Nat. Cell Biol.* **9**, 541 (2007).
6. Z. Darzynkiewicz *et al.*, *Cytometry* **13**, 795 (1992).
7. R. A. Harrison, S. E. Vickers, *J. Reprod. Fertil.* **88**, 343 (1990).
8. S. Zullig *et al.*, *Curr. Biol.* **17**, 994 (2007).
9. V. A. Fadok *et al.*, *J. Immunol.* **149**, 4029 (1992).
10. V. A. Fadok, D. Xue, P. Henson, *Cell Death Differ.* **8**, 582 (2001).
11. D. C. Royal *et al.*, *J. Biol. Chem.* **280**, 41976 (2005).
12. T. R. Zahn, M. A. Macmorris, W. Dong, R. Day, J. C. Hutton, *J. Comp. Neurol.* **429**, 127 (2001).
13. L. Timmons, D. L. Court, A. Fire, *Gene* **263**, 103 (2001).
14. N. Tavernarakis, S. L. Wang, M. Dorovkov, A. Ryazanov, M. Driscoll, *Nat. Genet.* **24**, 180 (2000).
15. M. E. Greenberg *et al.*, *J. Exp. Med.* **203**, 2613 (2006).
16. H. Bayir *et al.*, *Biochim. Biophys. Acta* **1757**, 648 (2006).
17. X. Wang *et al.*, *Science* **302**, 1563 (2003).
18. Z. Zhou, E. Hartwieg, H. R. Horvitz, *Cell* **104**, 43 (2001).
19. J. Yuan, S. Shaham, S. Ledoux, H. M. Ellis, H. R. Horvitz, *Cell* **75**, 641 (1993).
20. P. W. Reddien, S. Cameron, H. R. Horvitz, *Nature* **412**, 198 (2001).
21. D. J. Hoeppner, M. O. Hengartner, R. Schnabel, *Nature* **412**, 202 (2001).
22. T. Pomorski, A. K. Menon, *Cell. Mol. Life Sci.* **63**, 2908 (2006).
23. J. Ding *et al.*, *J. Biol. Chem.* **275**, 23378 (2000).
24. K. Balasubramanian, A. J. Schroit, *Annu. Rev. Physiol.* **65**, 701 (2003).
25. W. G. Kelly, S. Xu, M. K. Montgomery, A. Fire, *Genetics* **146**, 227 (1997).

26. We thank Y. Shi for help with constructs, A. Fire for the *ccIs4251* strain, J. Hutton for the *inIs179* strain, M. Hengartner for the *opIs117* strain, M. Driscoll for the *bzIs8* strain and the $P_{mec\text{-}4}$mCherry construct, and X. Xie and T. Blumenthal for comments on the manuscript. This work was supported by the Burroughs Wellcome Fund Career Award (D.X.), a grant from MEXT of Japan (S.M.), NIH grant R01 GM59083 (D.X.), and Human Frontier Science Program grant RGP0016/2005-C (D.X.).

Supporting Online Material

www.sciencemag.org/cgi/content/full/320/5875/528/DC1
Materials and Methods
SOM Text
Figs. S1 to S7
Tables S1 and S2
References and Notes

29 January 2008; accepted 11 March 2008
10.1126/science.1155847

Vaccinia Virus Uses Macropinocytosis and Apoptotic Mimicry to Enter Host Cells

Jason Mercer and Ari Helenius*

Viruses employ many different strategies to enter host cells. Vaccinia virus, a prototype poxvirus, enters cells in a pH-dependent fashion. Live cell imaging showed that fluorescent virus particles associated with and moved along filopodia to the cell body, where they were internalized after inducing the extrusion of large transient membrane blebs. p21-activated kinase 1 (PAK1) was activated by the virus, and the endocytic process had the general characteristics of macropinocytosis. The induction of blebs, the endocytic event, and infection were all critically dependent on the presence of exposed phosphatidylserine in the viral membrane, which suggests that vaccinia virus uses apoptotic mimicry to enter cells.

Poxviruses are enveloped DNA viruses that differ from other animal viruses in their large size and complexity (*1*). For humans, the most dangerous is variola virus, the causative agent of smallpox and one of most devastating pathogens in history. The development of new antiviral strategies against poxviruses will require detailed information about their replication cycle (*2*).

During replication, two infectious forms of vaccinia are produced: intracellular mature virus (MV) and extracellular enveloped virus (EV). The binding of MVs to cells involves cell-surface glycosaminoglycans (*3*), and MVs have been observed binding to actin-containing fingerlike protrusions (*4*). The viral envelope can fuse directly with the plasma membrane (*3*), but productive entry occurs mainly by low pH–dependent endocytosis into large uncoated vacuoles (*5*).

To follow the entry of individual virions, we generated MVs with an enhanced yellow fluorescent protein (EYFP)–tagged core protein [EYFP-CORE-MVs (*6*)]. When added to cells expressing enhanced green fluorescent protein (EGFP)–actin or enhanced cyan fluorescent protein–actin, virions that bound to filopodia moved toward the cell body (Fig. 1A and movies S1 to S3). As seen with other viruses (*7*), the movement was uninterrupted, with a rate approximating that of actin retrograde flow (1.05 ± 0.38 μm/min, fig. S1).

When MVs reached the cell body, a dramatic change occurred in the plasma membrane: A large, roughly spherical bleb (diameter 2 ± 0.57 μm; n = 42 blebs) extruded at the site of contact with the virus, followed by the formation of further blebs along the cell body. Each bleb remained extended for 10 ± 2 s (n = 42) before actin accumulated on the membrane, and the bleb retracted within 18 ± 3 s (n = 42) (Fig. 1B, movies S4 to S6, and figs. S2 and S3). Bleb retraction and cortical actin reassembly coincided with virus entry. Blebbing peaked 30 min after virus addition (Fig. 1C). The fraction of blebbing cells increased with the multiplicity of infection (MOI), while the number of blebs per blebbing cell remained in the range of 75 to 125 (Fig. 1, D and E, and fig. S4). Thus, a single incoming MV induced a generalized state in the cell that promoted bleb formation along the entire cell body.

To test whether blebbing was needed for infection, we used blebbistatin, an inhibitor of myosin II–dependent blebbing (*8*). Infection was quantified with EGFP-expressing MVs (EGFP-EXPRESS-MVs) and fluorescence-activated cell sorting (FACS) (fig. S5) (*6*). Blebbistatin prevented the formation of MV-induced blebs (fig. S6) and inhibited infection by 65% (Fig. 1F), which suggests that bleb formation was involved in productive entry.

In addition to actin, blebs contained Rac1, RhoA, ezrin, and cortactin (Fig. 1G), which are important for plasma membrane blebbing under other conditions (*9*) and for MV entry (*4*). MV-

ETH Zurich, Institute of Biochemistry, Schafmattstrasse 18, ETH Hönggerberg HPM E6.3 Zurich, Switzerland.

*To whom correspondence should be addressed. E-mail: ari.helenius@bc.biol.ethz.ch

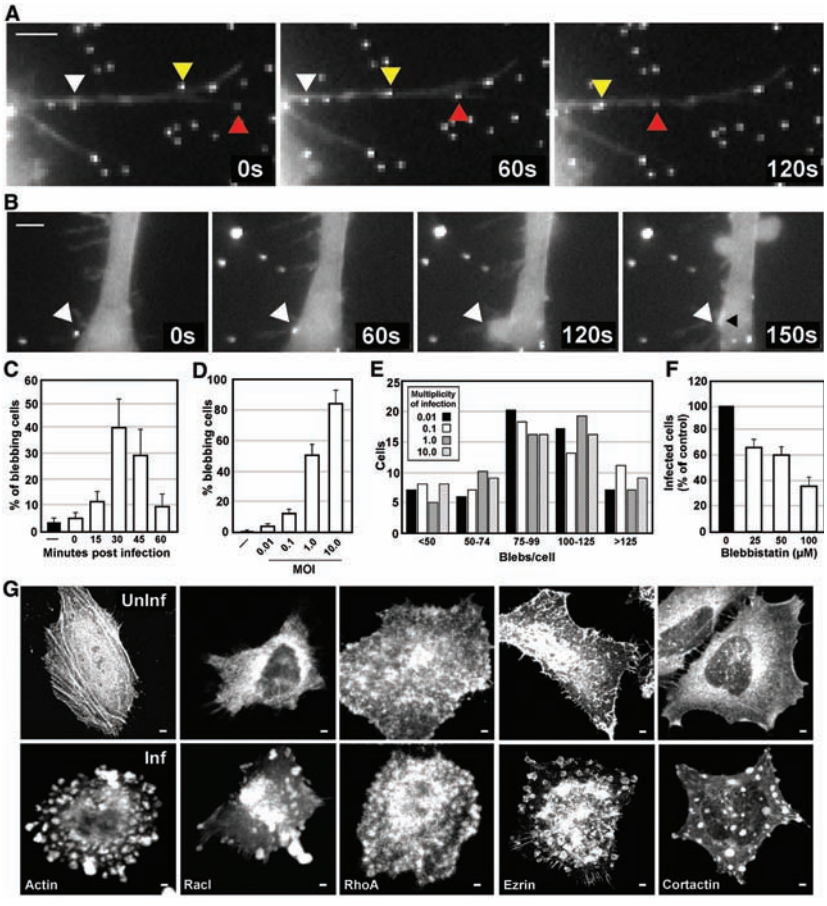

Fig. 1. Virion movement and membrane perturbation during MV entry. (**A**) EYFP-CORE-MVs were added to cells expressing GFP-actin. Arrowheads highlight virions. Scale bars, 2 μm (movies S1 to S3). (**B**) Imaging was performed as in (A). The virion of interest is indicated by the white arrowheads. The actin patch at the site of bleb collapse is indicated by a black arrowhead. Scale bars, 2 μm. (movies S4 to S6). (**C**) Infected cells were fixed at the indicated times and scored for blebbing. Data are means of triplicate experiments ± SD. (**D**) Cells infected at varying MOIs (0.01 to 10) were fixed 30 min after infection and blebbing cells were quantified (for images, see fig. S4). Data are means of triplicate experiments ± SD. (**E**) Blebbing cells from (D) were analyzed for the number of blebs per cell. Results of triplicate experiments are shown. (**F**) Confluent blebbistatin-treated cells were infected with EGFP-EXPRESS-MVs. Infection was determined by fluorescence-activated cell sorting (FACS) (*6*). Data are means of triplicate experiments ± SD. (**G**) Fluorescently tagged proteins were visualized in uninfected (uninf) and infected (inf) cells. Images are displayed as a maximum projected *z* stack of 10 confocal slices. Scale bars, 2 μm.

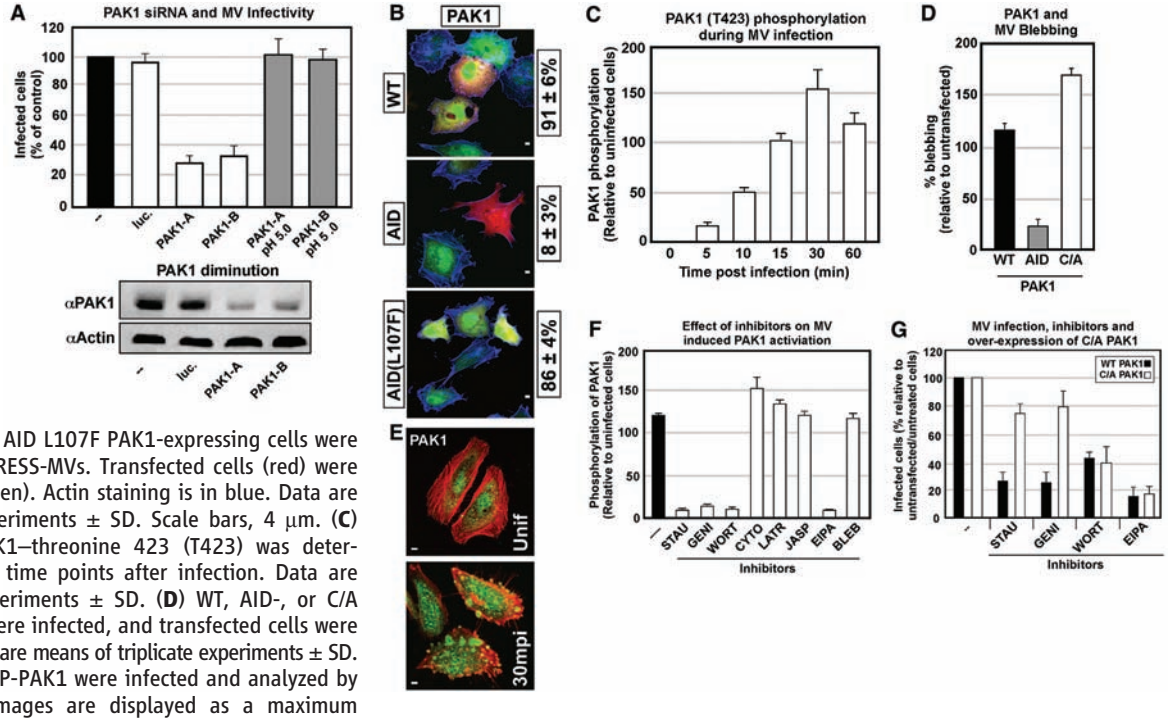

Fig. 2. PAK1 is required for blebbing and MV entry. (**A**) (Top) cells treated with mock (-), luciferase (luc), or two PAK1 siRNAs were infected with EGFP-EXPRESS-MVs. Acid bypass (*6*) of PAK1 siRNAs is shown (gray bars). Infectivity was determined by FACS (*6*) Data are means of triplicate experiments ± SD. (Bottom) Immunoblots of PAK1 and actin. (**B**) Wild-type (WT), AID-, or AID L107F PAK1-expressing cells were infected with EGFP-EXPRESS-MVs. Transfected cells (red) were scored for infection (green). Actin staining is in blue. Data are means of triplicate experiments ± SD. Scale bars, 4 μm. (**C**) Phosphorylation of PAK1—threonine 423 (T423) was determined at the indicated time points after infection. Data are means of triplicate experiments ± SD. (**D**) WT, AID-, or C/A PAK1-expressing cells were infected, and transfected cells were scored for blebbing. Data are means of triplicate experiments ± SD. (**E**) Cells expressing EGFP-PAK1 were infected and analyzed by confocal microscopy. Images are displayed as a maximum projected *z* stack of 10 confocal slices (*6*). Actin staining is in red. Scale bars, 4 μm. (**F**) Pretreated cells were infected with EGFP-EXPRESS-MVs. Lysates were analyzed for PAK1 phosphorylation. Data are means of triplicate experiments ± SD. Treatments were as follows: untreated (–), staurosporin (STAU), genistein (GENI), wortmannin (WORT), cytochalasin D (CYTO), latrunculin A (LATR), jaspakinolide (JASP), EIPA, and blebbistatin (BLEB). (**G**) Cells expressing WT or C/A PAK1 and pretreated with STAU, GENI, WORT, or EIPA were infected with EGFP-EXPRESS-MVs. Transfected cells were scored for infection. Data are means of triplicate experiments ± SD.

induced blebbing resembled that observed during cell motility, cytokinesis, and apoptosis (*9*–*11*).

Our investigations into the cellular factors required for MV blebbing and entry first focused on p21-activated kinase 1 (PAK1), an essential factor for MV infection. PAK1 is a serine-threonine kinase with a central role in cell motility (*12*). To validate the requirement for PAK1 in infection, we used two small interfering RNAs (siRNAs), which gave 82 and 76% knockdown of PAK1 protein (Fig. 2A, bottom). Infection was reduced by 74 and 68%, respectively (Fig. 2A, top). The PAK1 autoinhibitory domain (AID) inhibited infection by 83%, whereas an inactive AID (AID L107F) caused only a 5% reduction in infection (Fig. 2B). When MVs were added to cells, phosphorylation of threonine 423 of PAK1, which is essential for macropinocytosis (*13*), was detected (Fig. 2C).

Acid-mediated bypass (*6*) of PAK1 siRNA demonstrated that PAK1 was required for pre-fusion events (Fig. 2A, gray bars). PAK1 was also needed for blebbing: PAK1-AID reduced blebbing by 94%, whereas constitutive active (C/A T423E) PAK1 increased blebbing by 53% (Fig. 2D). Additionally, PAK1 localized into membrane blebs during infection (Fig. 2E).

Next, several perturbants were tested for effects on blebbing and infection, including dominant-negative (D/N) and C/A Rac1, C/A Arf6, and D/N dynamin-2, as well as inhibitors of RhoA, dynamin-2, PKC, serine, threonine, tyrosine- and PI 3-kinases (PI3Ks); Na^+/H^+ exchangers and macropinocytosis; endosomal fusion; actin dynamics; and blebbing.

Many perturbants inhibited both blebbing and infection, confirming that the two processes are linked. Both were dependent on tyrosine, serine-threonine, and PI3Ks; Na^+/H^+ exchangers; actin; Rac1; and PAK1 (Figs. 2 and 3, figs. S6 to S8, and table S1). After acid bypass, the inhibitors failed to block infection, indicating that each affected pre-fusion steps (Fig. 3C, pH 5.0). Bypass of monensin and bafilomycin A1 has been demonstrated (*5*). C/A Arf6 inhibited infection by 78% (Fig. 3D), whereas D/N dynamin 2 and dynasore had no impact (Fig. 3E and fig. S7).

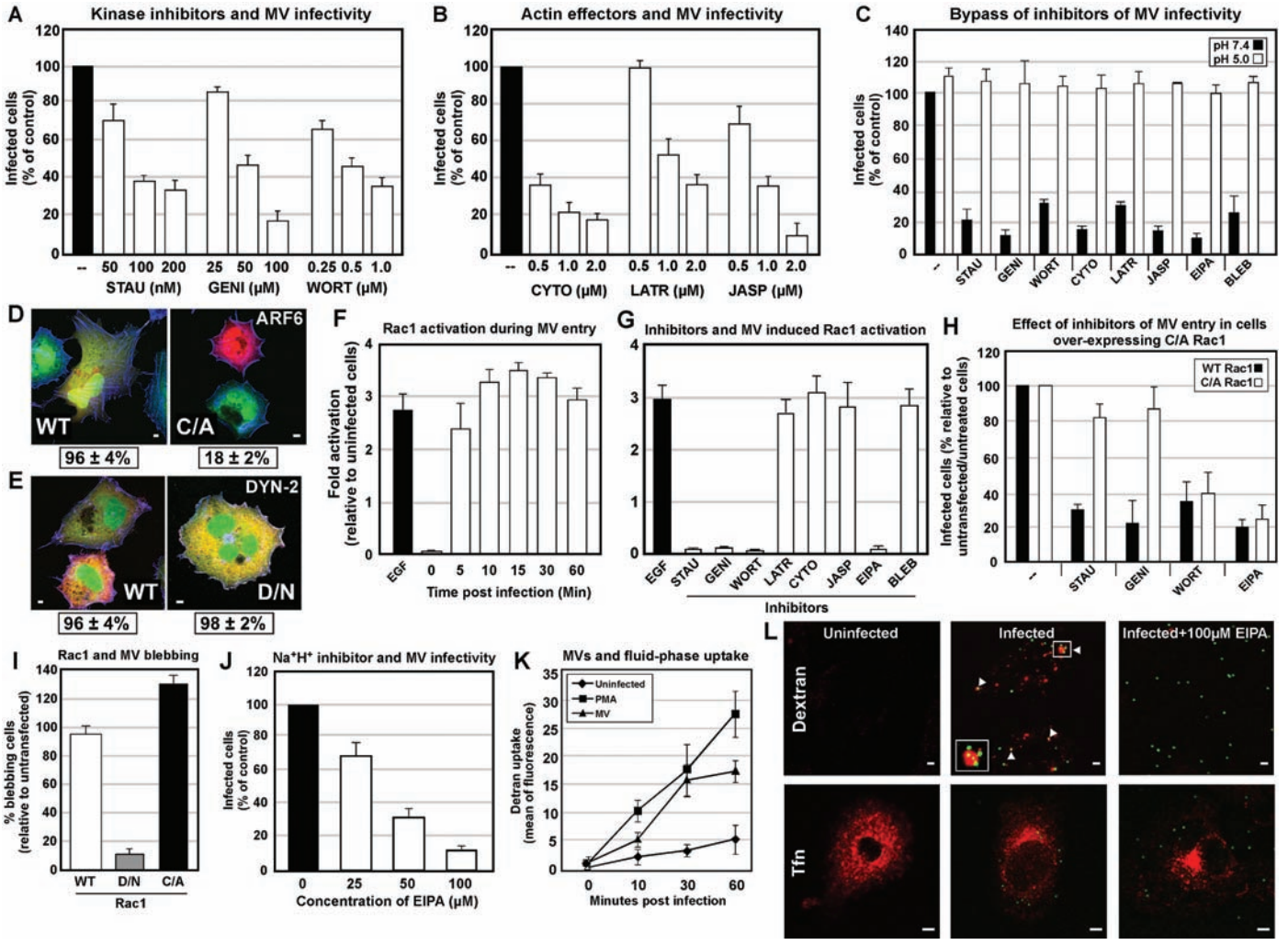

Fig. 3. MVs use macropinocytosis to enter cells. (**A** and **B**) The effect of kinase inhibitors and actin effectors on infectivity was assayed with FACS (*6*). Data are means of triplicate experiments ± SD. (**C**) Acid-mediated bypass was performed on inhibitor-treated infected cells. Infection was scored by FACS (*27*). Data are means of triplicate experiments ± SD. Abbreviations are as in Fig. 2F. (**D** and **E**) Cells expressing WT or mutant (C/A or D/N) Arf6 or Dyn 2 were infected with EGFP-EXPRESS-MVs. Cells were analyzed as in Fig. 2B (*28*). Data are means of triplicate experiments ± SD. Scale bars, 4 μm. (**F**) Activation of Rac1 was assessed at the indicated times [Cytoskeleton, Denver, CO (*6*)]. Data are means of triplicate experiments ± SD. (**G**) Experiments were performed as in Fig. 2F and analyzed as above. Inhibitors are abbreviated as in Fig. 2F. (**H**) Experiments were performed as in Fig. 2G. Data are means of triplicate experiments ± SD. (**I**) WT, D/N-, or C/A Rac1–expressing cells were infected with MVs. Transfected cells were scored for blebbing. Data are means of triplicate experiments ± SD. (**J**) Cells pretreated with EIPA were infected with EGFP-EXPRESS-MVs and analyzed by FACS (*6*). Data are means of triplicate experiments ± SD. (**K**) MV-infected cells were pulsed with 488-dextran 10 min before being harvested. Cells were analyzed by FACS (*6*) Untreated (negative control) and PMA (positive control) are shown. Data are means of triplicate experiments ± SD. (**L**) EYFP-CORE-MVs were internalized in the presence of 70-kD 568-dextran or 568-transferrin (Tfn). Cells were visualized for virions (green) and dextran or Tfn (red). The effect of EIPA treatment was assessed in parallel. Scale bars, 4 μm.

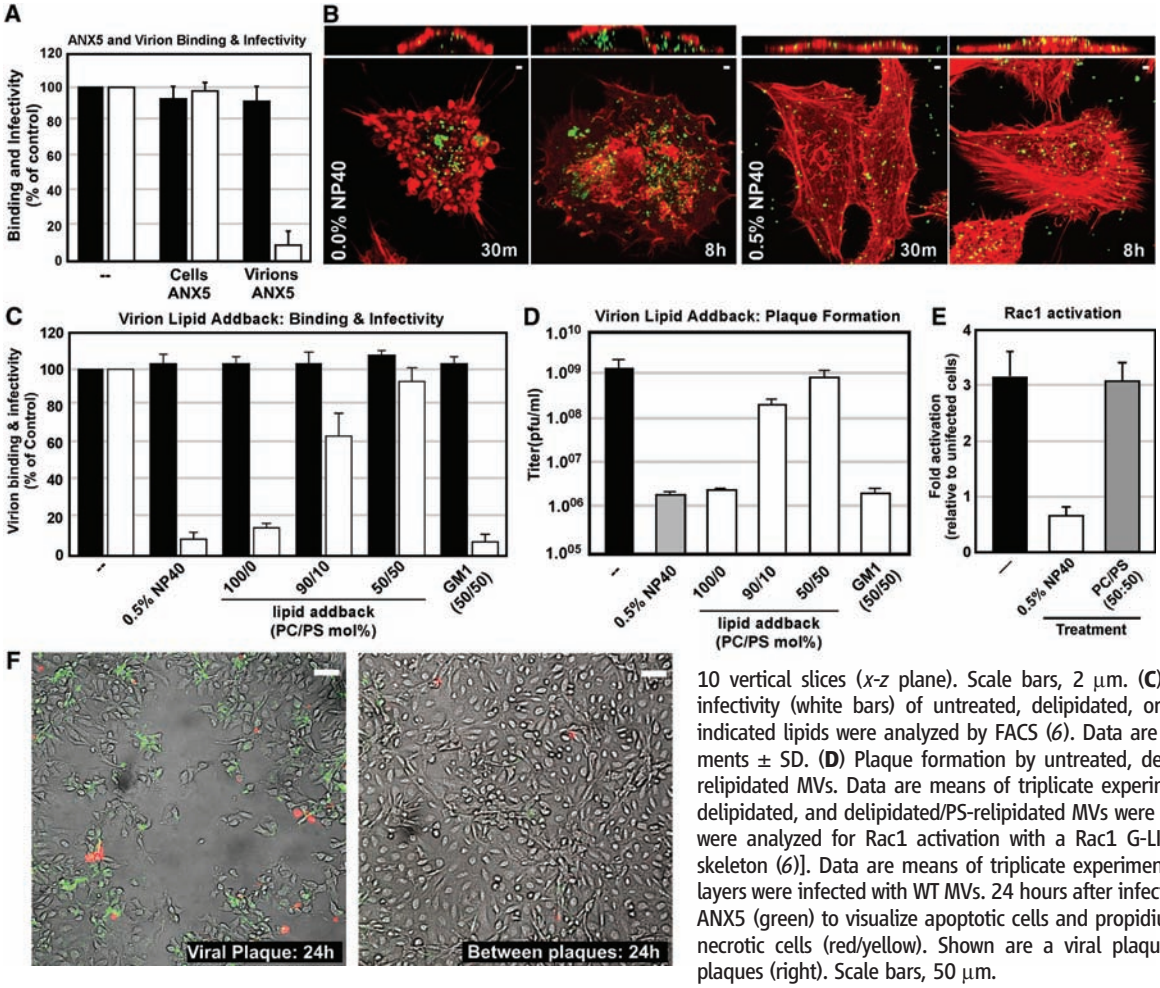

Fig. 4. PS is required for MV-induced signaling and internalization. (**A**) Cells or EYFP-CORE-MVs/EGFP-EXPRESS-MVs were pretreated with untagged ANX5 (*6*). Treated cells (cells ANX5) and virions (virions-ANX5) were analyzed for viron binding (black bars) and infection (white bars) by FACS (*6*). Data are means of triplicate experiments ± SD. (**B**) Cells were infected with untreated or delipidated EYFP-CORE-MVs (green) and fixed 30 min or 8 hours after virus addition. Cells were stained for actin (red), and visualized. (Bottom) Maximum *z* projection of 10 horizontal slices (*x-y* plane). (Top) Maximum *z* projection of 10 vertical slices (*x-z* plane). Scale bars, 2 μm. (**C**) Binding (black bars) and infectivity (white bars) of untreated, delipidated, or MVs relipidated with the indicated lipids were analyzed by FACS (*6*). Data are means of triplicate experiments ± SD. (**D**) Plaque formation by untreated, delipidated, and delipidated/relipidated MVs. Data are means of triplicate experiments ± SD. (**E**) Untreated, delipidated, and delipidated/PS-relipidated MVs were used to infect cells. Lysates were analyzed for Rac1 activation with a Rac1 G-LISA Activation Assay [Cytoskeleton (*6*)]. Data are means of triplicate experiments ± SD. (**F**) BSC40 monolayers were infected with WT MVs. 24 hours after infection, cells were stained with ANX5 (green) to visualize apoptotic cells and propidium iodide (red) to visualize necrotic cells (red/yellow). Shown are a viral plaque (left) and cells between plaques (right). Scale bars, 50 μm.

Rac1, a regulatory guanosine triphophatase of PAK1, was activated during MV entry (Fig. 3F). Staurosporin, genistein, wortmannin, and 5-*N*-ethyl-*N*-isopropyl-amiloride (EIPA) prevented activation of PAK1 and Rac1, whereas actin effectors and blebbistatin did not (Figs. 2F and 3G). C/A Rac1 and PAK1 restored infection in the presence of staurosporin and genistein but not wortmannin or EIPA (Figs. 2G and 3H). These results are consistent with the need for tyrosine and possibly serine–/threonine kinase, PI3K and Na^+/H^+ exchange upstream of PAK1 and Rac1, and downstream PI3K and Na^+/H^+ exchange activity. Additionally, D/N Rac1 inhibited blebbing 84%, and C/A Rac1 increased blebbing 30% (Fig. 3I). Although activated during infection (fig. S8A), RhoA inhibition did not prevent blebbing (fig. S8B) but accelerated infection as previously demonstrated (fig. S8, C and D) (*4*, *14*).

With this perturbation pattern, it was likely that MVs were using macropinocytosis (table S1 and Fig. 3) (*15*, *16*). Sensitivity to inhibitors of Na^+/H^+ exchangers is a characteristic of this pathway (*17*). With 85% inhibition of infectivity, EIPA was the most efficient inhibitor tested (Fig. 3J).

Consistent with macropinocytosis, internalization of 488-dextran was elevated fivefold within 30 min of MV addition (Fig. 3K). Microscopy showed that MVs co-internalized with a fluid-phase (568-dextran), but not a clathrin-mediated (568-transferrin), marker (Fig. 3L).

MVs may use macropinocytosis because of their large size. With few exceptions (*18*), pathogens the size of vaccinia are not internalized by clathrin- or caveolin/raft-mediated endocytosis. However, MVs are comparable in size to apoptotic bodies that are macropinocytosed by professional phagocytes and other cell types (*19*, *20*). The uptake of apoptotic debris is triggered by surface-exposed phosphatidylserine (PS) (*19*).

The MV membrane has been shown to be enriched in PS (36%) (*21*, *22*), and PS is required for infectivity (*23*). When exposed to 647-ANX5, a PS-binding protein, EYFP-CORE-MVs are stained, indicating that PS is exposed on the MV surface (fig. S9). When MV PS was masked with ANX5, infectivity (white bars) was inhibited by 90% without affecting binding (black bars) (Fig. 4A, virions ANX 5). Binding and infectivity were not affected when cells were pretreated with ANX5 (Fig. 4A, cells ANX 5).

To assess the role of viral PS, we treated MVs with Nonidet-P40 (NP-40), which causes a total loss of viral lipid and a dramatic drop in infectivity at a concentration of 0.5% or higher (fig. S10) (*21*, *24*). Extracted virions could bind cells, but they did not induce blebbing or entry (Fig. 4B, 30 min). After 8 hours, extracted MVs were still at the cell surface with no evidence of viral cytopathic effects, MV entry, or replication (Fig. 4B, 8 hours).

Using established methods (*21*), we restored phosphatidylcholine (PC) and varying amounts of PS (0, 10, or 50 mol %) to delipidated viruses. Restoration of PS was confirmed by ANX5 binding (fig. S9). Relipidated MVs bound cells normally (black bars), but only PS-reconstituted viruses exhibited restored infectivity and plaque formation (Fig. 4C, white bars, and Fig. 4D) (*21*). Liposomes containing another negatively charged lipid, ganglioside GM1, did not restore infectivity.

Additionally, delipidated MVs were highly attenuated for Rac1 activation, whereas PS-relipidated MVs (50 mol %) restored Rac1 activation to control levels (Fig. 4E). Thus, viral PS might be analogous to cellular PS in the elimination of apoptotic bodies.

Finally, we analyzed whether vaccinia-infected cells underwent apoptosis or necrosis. Cells at the edge of viral plaques displayed exposed PS (green), a hallmark of apoptosis (*27*), whereas few cells were necrotic (red) (Fig. 4F, left), suggesting that late-stage vaccinia-infected cells undergo apoptosis. Cells between plaques were neither apoptotic nor necrotic (Fig. 4F,

right). MV spread is therefore likely to be connected with apoptosis and a preprogrammed macropinocytic response of neighboring cells to apoptotic bodies.

Vaccinia MVs use macropinocytosis and apoptotic mimicry to enter host cells. There are several advantages of using this entry strategy. First, it permits endocytic internalization of particles too big for other viral endocytic mechanisms. Second, it allows the virus to enter many different cell types, because PS-mediated clearance of apoptotic material is common to most cells (*19*, *26*). Finally, by mimicking an apoptotic body, MVs may avoid immune detection as they spread to surrounding cells, because macropinocytosis of apoptotic debris suppresses the activation of innate immune responses (*26*). The lack of macrophage infiltration and T cell maturation during murine lung infection by vaccinia (*27*) may be explained by this "silent" mechanism of cell-to-cell spread.

References and Notes

1. B. Moss, D. M. Knipe, P. M. Howley, *Fields Virology* (Lippincott-Raven, Philadelphia, PA, 2007), vol. 5.
2. S. C. Harrison *et al.*, *Proc. Natl. Acad. Sci. U.S.A.* **101**, 11178 (2004).
3. G. C. Carter, M. Law, M. Hollinshead, G. L. Smith, *J. Gen. Virol.* **86**, 1279 (2005).
4. J. K. Locker *et al.*, *Mol. Biol. Cell* **11**, 2497 (2000).
5. A. C. Townsley, A. S. Weisberg, T. R. Wagenaar, B. Moss, *J. Virol.* **80**, 8899 (2006).
6. Materials and methods are available as supporting material on *Science* Online.
7. M. J. Lehmann, N. M. Sherer, C. B. Marks, M. Pypaert, W. Mothes, *J. Cell Biol.* **170**, 317 (2005).
8. J. Limouze, A. F. Straight, T. Mitchison, J. R. Sellers, *J. Muscle Res. Cell Motil.* **25**, 337 (2004).
9. G. T. Charras, C. K. Hu, M. Coughlin, T. J. Mitchison, *J. Cell Biol.* **175**, 477 (2006).
10. D. J. Fishkind, L. G. Cao, Y. L. Wang, *J. Cell Biol.* **114**, 967 (1991).
11. J. C. Mills, N. L. Stone, J. Erhardt, R. N. Pittman, *J. Cell Biol.* **140**, 627 (1998).
12. M. C. Parrini, M. Matsuda, J. de Gunzburg, *Biochem. Soc. Trans.* **33**, 646 (2005).
13. S. Dharmawardhane *et al.*, *Mol. Biol. Cell* **11**, 3341 (2000).
14. F. Valderrama, J. V. Cordeiro, S. Schleich, F. Frischknecht, M. Way, *Science* **311**, 377 (2006).
15. S. Mayor, R. E. Pagano, *Nat. Rev. Mol. Cell Biol.* **8**, 603 (2007).
16. S. B. Sieczkarski, G. R. Whittaker, *J. Gen. Virol.* **83**, 1535 (2002).
17. M. A. West, M. S. Bretscher, C. Watts, *J. Cell Biol.* **109**, 2731 (1989).
18. E. Veiga, P. Cossart, *Nat. Cell Biol.* **7**, 894 (2005).
19. P. M. Henson, D. L. Bratton, V. A. Fadok, *Curr. Biol.* **11**, R795 (2001).
20. N. Platt, R. P. da Silva, S. Gordon, *Trends Cell Biol.* **8**, 365 (1998).
21. Y. Ichihashi, M. Oie, *Virology* **130**, 306 (1983).
22. H. T. Zwartouw, *J. Gen. Microbiol.* **34**, 115 (1964).
23. M. Oie, *Virology* **142**, 299 (1985).
24. Y. Ichihashi, M. Oie, T. Tsuruhara, *J. Virol.* **50**, 929 (1984).
25. S. J. Martin *et al.*, *J. Exp. Med.* **182**, 1545 (1995).
26. M. L. Albert, *Nat. Rev. Immunol.* **4**, 223 (2004).
27. D. Hayasaka, F. A. Ennis, M. Terajima, *Virol. J.* **4**, 22 (2007).

28. We thank P. Traktman for providing viruses; H. Ewers for the production of liposomes; R. Sacher, B. Snijder, and L. Pelkmans for assistance with siRNA screening; and the members of the Helenius lab for helpful discussion. Funding was obtained from ETH Zurich and the Roche Foundation.

Supporting Online Material

www.sciencemag.org/cgi/content/full/320/5875/531/DC1
Materials and Methods
Figs. S1 to S10
Table S1
References
Movies S1 to S6

11 January 2008; accepted 29 February 2008
10.1126/science.1155164

Encoding Gender and Individual Information in the Mouse Vomeronasal Organ

Jie He,[1] Limei Ma,[1] SangSeong Kim,[1] Junichi Nakai,[2] C. Ron Yu[1]*

The mammalian vomeronasal organ detects complex chemical signals that convey information about gender, strain, and the social and reproductive status of an individual. How these signals are encoded is poorly understood. We developed transgenic mice expressing the calcium indicator G-CaMP2 and analyzed population responses of vomeronasal neurons to urine from individual animals. A substantial portion of cells was activated by either male or female urine, but only a small population of cells responded exclusively to gender-specific cues shared across strains and individuals. Female cues activated more cells and were subject to more complex hormonal regulations than male cues. In contrast to gender, strain and individual information was encoded by the combinatorial activation of neurons such that urine from different individuals activated distinctive cell populations.

Pheromones are a group of chemicals critical for social communication in many animal species (*1*, *2*). Information on sex, strain, social rank, reproductive status, and terrestrial ownership is represented in the complex pheromone components in urine and bodily secretions. In mice, detection of such complex chemical signals by the vomeronasal organ (VNO) and the olfactory epithelium plays an important role in triggering endocrine changes and eliciting innate territorial aggression and mating behaviors (*3*–*5*). The rodent VNO expresses more than 250 receptors that detect pheromones and transmit the signals to the brain (*6*–*11*). It is not well understood how these neurons encode information about gender and individuals. Urine contains hundreds or even thousands of substances, only a handful of which have been identified as putative pheromones (*12*–*16*). The complexity of natural pheromone signals poses a challenge to our understanding of what information is transmitted to the vomeronasal neurons (*17*, *18*).

Each vomeronasal neuron expresses only one of the ~250 estimated pheromone receptor genes (*6*–*9*, *19*, *20*), and the receptor's activation elevates intracellular calcium (*21*). To visualize pheromone-induced activity in a large population of neurons, we generated tetO-G-CaMP2 transgenic mouse lines (*22*–*24*). When crossed to animals carrying the OMP-IRES-tTA allele (*25*), G-CaMP2 expression was restricted to the neurons in the olfactory system (Fig. 1, A and B, and Movie S1). Electrophysiological properties of the G-CaMP2–expressing VNO neurons, as well as their response to pheromones, were indistinguishable from those of the controls (fig. S1). The projection patterns of the sensory neurons and the innate mating and aggressive behaviors of the G-CaMP2 mice were also indistinguishable from those of wild-type and littermate control animals (figs. S2 to S5).

In VNO slices prepared from 2- to 6-month-old male or female animals, application of diluted urine elicited an increase in fluorescence in ~30 to 40% of G-CaMP2–positive neurons, some of which showed gender-specific responses (Fig. 1C and Movies S2 and S3). We did not observe significant differences between slices from male and female animals in detecting the gender-specific cues. Prolonged applications of urine elicited prolonged calcium increases (Fig. 1D). This nonadaptive nature of the responses was in agreement with electrophysiological recordings reported previously (*17*, *26*). In addition, the responses were dose dependent and were blocked by 2-APB and U71344, inhibitors of signaling pathways downstream of pheromone receptor activation (*21*, *27*) (Fig. 1, C and D, and fig. S7). Thus, the expression of G-CaMP2 provided us an easy and sensitive method to examine population responses of VNO neurons to multiple urine samples.

Initial analyses of VNO neuron response to male and female urine pooled from multiple individuals of the C57BL/6 strain showed that ~15% of G-CAMP2–positive cells responded to both male and female urine. About 8% and 12% of the cells

[1]Stowers Institute for Medical Research, 1000 East 50th Street, Kansas City, MO 64110, USA. [2]Laboratory for Memory and Learning, RIKEN Brain Science Institute, 2-1 Hirosawa, Wakoshi, Saitama, 351-0198, Japan.

*To whom correspondence should be addressed: cry@stowers-institute.org